ACS APPLIED MATERIALS & INTERFACES

Research Article

www.acsami.org

Metal–Organic Framework Derived $ZnO/ZnFe_2O_4/C$ Nanocages as Stable Cathode Material for Reversible Lithium–Oxygen Batteries

Wei Yin, Yue Shen,* Feng Zou, Xianluo Hu, Bo Chi, and Yunhui Huang*

State Key Laboratory of Material Processing and Die & Mould Technology, School of Materials Science and Engineering, Huazhong University of Science and Technology, Wuhan, Hubei 430074, People's Republic of China

Supporting Information

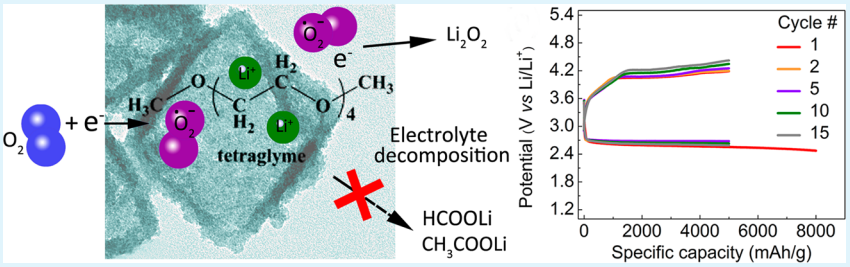

ABSTRACT: Tremendous efforts have been devoted to exploring various Li–O_2 cathode catalysts for oxygen reduction reaction (ORR) and oxygen evolution reaction (OER). However, most of the high-activity ORR/OER catalysts can also accelerate side-reactions, such as electrolyte degradation on cycling. To address this issue, we change our strategy from pursuing highly active catalysts to developing stable cathodes that are compatible with the electrolyte. In this work, hierarchical mesoporous $ZnO/ZnFe_2O_4/C$ (ZZFC) nanocages are synthesized from the templates of metal–organic framework (MOF) nanocages. Such ZZFC nanocages have lower ORR/OER catalytic activity as compared with the widely used catalysts for fuel cells, but they do not catalyze the degradation of organic electrolyte during operation. Furthermore, the optimized porosity and conductivity can fit well the needs of the Li–O_2 cathode. When employed in a Li–O_2 battery, the ZZFC cathode delivers a primary discharge/charge capacity exceeding 11 000 mAh g^{-1} at a current density of 300 mA g^{-1} and an improved cyclability with capacity of 5000 mAh g^{-1} for 15 cycles. The superior electrochemical performance is ascribed to the hierarchical porosity and little degradation of the organic electrolyte.

KEYWORDS: *metal–organic framework, stable nanocage catalyst, hierarchical pores, nonaqueous electrolyte, lithium–oxygen battery*

1. INTRODUCTION

Rechargeable lithium–oxygen batteries (LOBs) have received worldwide attention due to their ultrahigh theoretical specific capacity far exceeding conventional lithium-ion batteries.[1,2] Cycle performance is one of the main concerns for practical application of LOBs. The cyclability strongly depends on the reversibility of Li_2O_2 formation and oxidation reactions on the cathode.[3−6] At present, the oxygen cathodes in most LOBs consist of porous carbon substrate (e.g., graphene,[7,8] carbon nanotubes,[9,10] pyrolytic carbon[11−13]) and/or catalyst.[14−18] However, there are still some roadblocks for practical implementation related to the porous oxygen-cathode materials.[19−22] For instance, the generally used catalysts indeed promote the kinetics of ORR and OER, but they also accelerate other undesirable reactions: superoxide radicals, an intermediate of the oxygen reduction reaction, may attack the cathode and organic electrolyte to make them irreversibly decompose upon cycling.[23−28] Consequently, the accumulation of by-products from these reactions (e.g., lithium alkyl carbonates, lithium carboxylates and Li_2CO_3) leads to a decreased round-trip efficiency and fast capacity decay.[26,29−33] To address this issue, some stable cathode designs have been proposed. For example, Au[34] and TiC[35] were used to reduce the side reactions and improve the cyclability in a DMSO-based electrolyte. Making cathodes electrochemically stable is a promising strategy to achieve high-performance LOBs.

On the other hand, considering that formation and decomposition of peroxide product in LOBs do not involve O–O bond breaking or formation, which is rather different from the ORR/OER processes in traditional hydrogen fuel cells, requirements of the catalysts for LOBs are also different from those for fuel cells. Principles for choosing the fuel-cell ORR catalysts, such as the "volcano" curve,[36−38] are no longer applicable in LOBs. Some weak catalysts that are unable to split O–O bond may be good enough for LOBs. Meanwhile, the porous structure of the cathode becomes more important in LOBs than in fuel cells. The multiphase interfacial discharge and charge reactions need hierarchical meso- and macropores to transport the reactants/electrons and to accommodate the Li_2O_2.[39,40]

In this work, hierarchical porous $ZnO/ZnFe_2O_4/C$ nanocages (abbreviated as ZZFC) derived from metal–organic

Received: December 28, 2014
Accepted: February 17, 2015
Published: February 17, 2015

DOI: 10.1021/am509143t
ACS Appl. Mater. Interfaces 2015, 7, 4947–4954

Table 1. Conductivity of the as-Synthesized Fe(III)-MOF-5 and the Samples Sintered at Different Temperatures in N_2

temperature (°C)	Fe(III)-MOF-5	400	450	500	550	600
conductivity (S cm^{-1})	$<5 \times 10^{-10}$	7.5×10^{-6}	2×10^{-6}	5×10^{-5}	1.5×10^{-5}	2×10^{-4}

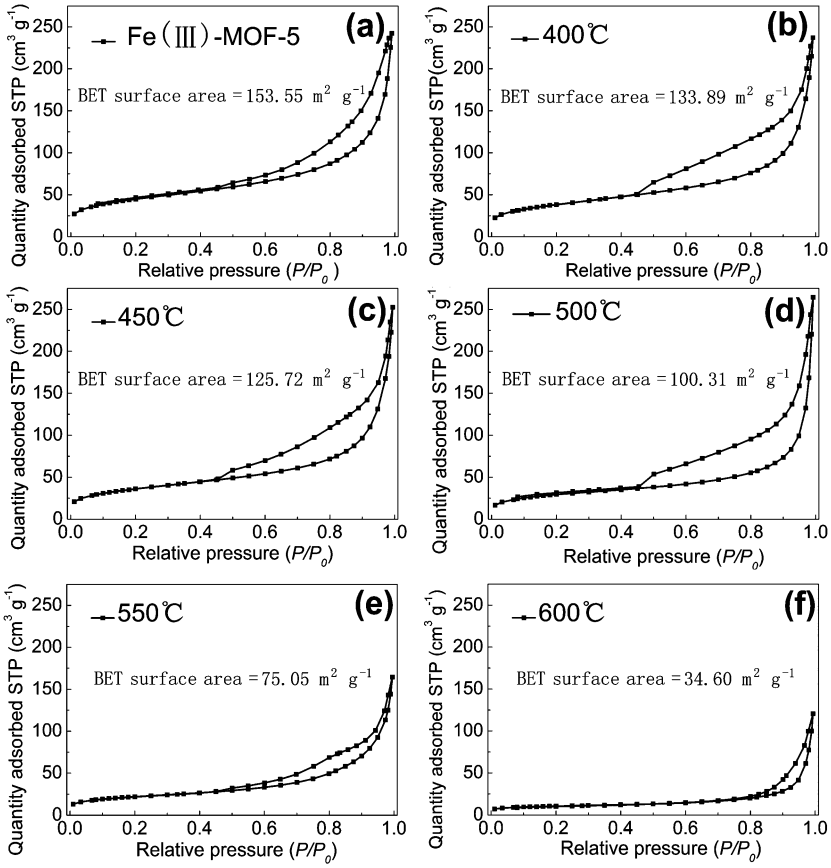

Figure 1. N_2 adsorption and desorption isotherms of the as-synthesized Fe(III)-MOF-5 and the samples after sintering in N_2 at various temperatures: (a) Fe(III)-MOF-5 precursor, (b) 400 °C, (c) 450 °C, (d) 500 °C, (e) 550 °C, and (f) 600 °C.

framework (MOF) nanocage templates were fabricated and tested as lithium−oxygen cathodes. Via an optimized pyrolysis process, the hollow octahedral shape of the MOF nanocages was maintained, and the walls of the nanocages became mesoporous and conductive. This unique architecture can provide a good cathode-Li_2O_2 contact during the OER process. When operated at high potential in pure oxygen atmosphere, the ZZFC electrode exhibited good stability in contact with tetraethylene glycol dimethyl ether (TEGDME)-based electrolyte, and almost no electrolyte degradation was detected. Compared with other cathode catalysts, the ZZFC has a weaker catalytic activity, but still delivers a high reversible capacity.

2. EXPERIMENTAL SECTION

2.1. Chemicals. Iron(III) acetylacetonate was purchased from Shanghai Dibo Chem. Tech. Co., Ltd.; Terephthalic acid, polyvinylpyrrolidone (PVP), zinc nitrate hexahydrate ($Zn(NO_3)_2{\cdot}6H_2O$), dimethylformamide, and ethanol were purchased from Sinopharm (Shanghai) Chem. Reagent Co., Ltd., China. Perdeuteriodimethyl sulfoxide was purchased from Cambridge Osotope Laboratories, Inc., USA. Anhydrous tetraethylene glycol dimethyl ether was purchase from Sigma-Aldrich Inc., USA, and was further dried with activated molecular sieves (type 4A). All chemical reagents were of analytical grade and used without any further purification. Carbon paper (CNFTP005) was purchased from Kunming NaTai Energy Co., Ltd., China.

2.2. Fabrication of ZnO/$ZnFe_2O_4$/C Nanocages. ZnO/$ZnFe_2O_4$/C nanocages were fabricated from octahedral Fe(III)-MOF-5 templates. The templates were synthesized via a reflux method as reported elsewhere.[41,42] In a typical process, 1.08 g of Fe(III) acetylacetonate ($Fe(acac)_3$), 0.835 g of $Zn(NO_3)_2{\cdot}6H_2O$, 0.17 g of terephthalic acid, and 3.6 g of polyvinylpyrrolidone (M_w = 55 000) were added into 240 mL of mixed solvent (dimethylformamide:ethanol = 5:3), followed by being stirred for 10 min to make them fully dissolved. The mixture was then transferred into a 500 mL three-necked flask and refluxed at 100 °C for 6 h. A dark orange precipitate was collected, washed with dimethylformamide and ethanol for several times, and dried at 80 °C for 24 h. The ZZFC nanocages were attained by heating the as-obtained Fe(III)-MOF-5 templates to various target temperatures in N_2 atmosphere at a heating rate of 1 °C min^{-1} and then directly cooled naturally down to room temperature.[42]

2.3. Characterizations. Nitrogen adsorption and desorption measurements were carried out on a Micromeritics ASAP 2020 system at 78 K. The specific surface area of the samples was calculated using the Brunauer−Emmet−Teller (BET) method, and the average pore diameter was determined with the desorption branch by the Barrett−Joyner−Halenda (BJH) model. The conductivity was measured with a direct-current resistivity method. The scanning electron microscopy (SEM) images and the energy dispersive X-ray spectroscopy (EDX) data of the samples were obtained with a Sirion 200 microscope. Transmission electron microscopy (TEM) and high-resolution TEM (HR-TEM) images were recorded by a JEOL microscope (JEM-2010F, Japan). X-ray diffraction (XRD) patterns were collected using a multipurpose diffractometer (Panalytical X'pert

DOI: 10.1021/am509143t
ACS Appl. Mater. Interfaces 2015, 7, 4947−4954

PRO MRD, Holland) with high-intensity Cu $K\alpha_1$ irradiation (λ = 1.5406 Å). The discharged and charged products were washed with anhydrous dimethyl sulfoxide and dried before characterization. X-ray photoelectron spectroscopy (XPS) measurement was performed on a VG MultiLab 2000 system with a monochromatic Al $K\alpha_1$ X-ray source (ThermoVG Scientific). Raman spectra were collected on a Lab RAM HR800 (Horiba JobinYvon) using a 532 nm laser. Thermogravimetric (TG) analysis was performed with a PerkinElmer Diamond apparatus at a heating rate of 10 °C min^{-1} in flowing air or N_2. For ^1H nuclear magnetic resonance (NMR) analysis, the discharged and charged electrodes were dipped in perdeuteriodimethyl sulfoxide to prepare the sample, and then the extracted solution was examined on a Bruker AscendTM 600 MHz spectrometer.

2.4. Electrochemical Measurements. All cyclic voltammetry (CV) and linear sweep voltammetry (LSV) tests were performed on an electrochemical workstation (CHI760E, CH Instruments, Shanghai, China) with a rotating disk system (Pine Research Instrumentation, USA). A glassy carbon (GC) disk electrode with a diameter of 5 mm was used as the working electrode. Metallic lithium pellets were used as the counter electrode and reference electrode. All electrochemical measurements were carried out in N_2- or O_2-saturated 1.0 mol l^{-1} LiTFSI (bistrifluoromethanesulfonimide lithium salt) in TEGDME solution at room temperature.

To prepare the working electrode, the GC electrode was first polished to mirror flat with alumina powder before use, and then different air cathode materials were loaded onto the GC electrode. 4.0 mg of active material, 0.5 mg of super P, and 10 μL 0.05 g mL^{-1} of polyvinylidene fluoride *N*-methyl pyrrolydone solution were mixed and ground to form sticky homogeneous slurry. 1 μL of the as-prepared slurry was loaded onto the GC electrode surface and dried at 80 °C for 24 h.

Lithium−oxygen coin batteries were assembled in argon-filled glovebox with oxygen and water contents less than 1 ppm. The battery consists of metallic lithium foil anode (0.5 mm thick), glass fiber separator (from Whatman), electrolyte of 1 mol l^{-1} LiTFSI in TEGDME, and as-synthesized cathode. A cathode slurry was prepared by mixing 80 wt % ZZFC, 10 wt % super P, and 10 wt % polyvinylidene fluoride (PVDF) in *N*-methyl pyrrolydone (NMP). The mixture was then coated onto a carbon paper by screen printing, followed by drying at 80 °C for 24 h in a vacuum oven. The carbon paper was then cut into circular discs with a diameter of 8 mm (0.5 cm^2). The same method was employed to prepare the pure super P electrode that consists of 90 wt % super P and 10 wt % PVDF. The mass loading of the cathode (super P + active material) was 0.4 mg cm^{-2}.

Galvanostatic discharge and charge performances of the LOBs were measured by a Land CT2001A battery system at a current density of 300 mA g^{-1} within a voltage range from 2.0 to 4.5 V in a plastic box filled with high purity oxygen. We also discharged and charged the batteries at a fixed capacity of 5000 mAh g^{-1} to test the cycling performance.

3. RESULTS AND DISCUSSION

An ideal LOB cathode should include a conductive porous framework. Very recently, some works have demonstrated that MOF-derived materials show a potential application as cathodes for LOBs due to their porous matrix. Wu et al. selected five different MOF open architectures as the O_2 electrodes for the first time.[43] However, without a postannealing process, the low conductivity limited the electrochemical performance. Chen et al. synthesized γ-Fe_2O_3/carbon nanocomposite air cathode by pyrolyzing a MIL-100-Fe MOF at 600 °C; the conductivity was raised after carbonization process, and hence the electrochemical performance was improved.[44] On the other hand, it is well-known that high temperature annealing leads to large particle size and low porosity. So we first optimized the annealing temperature to get good conductivity, and meanwhile to retain a suitable porous architecture. The

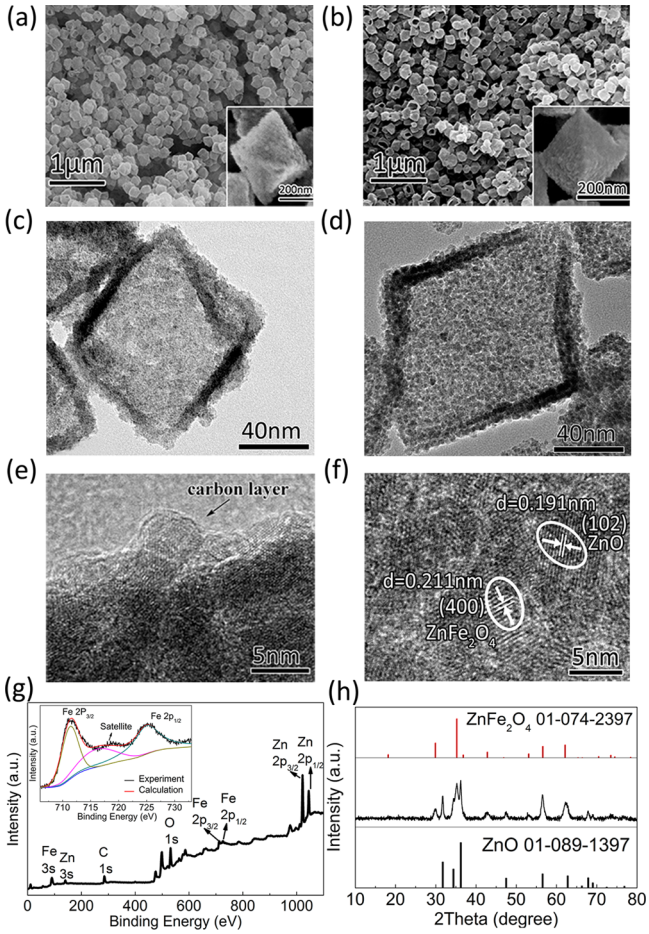

Figure 2. (a,b) SEM images of Fe(III)-MOF-5 (a) and ZZFC (b). (c,d) TEM images of Fe(III)-MOF-5 (c) and ZZFC (d). (e, f) high-resolution TEM images of ZZFC. (g) XPS spectra of ZZFC: survey spectrum. Inset: high-resolution XPS spectrum for Fe 2p. (h) XRD patterns of ZZFC.

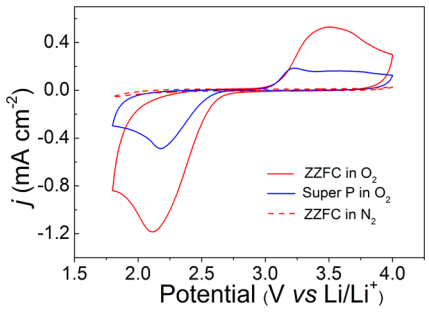

Figure 3. CVs of ORR/OER in 1.0 M LiTFSI in TEGDME on 80% ZZFC+10% super P+10% PVDF (red solid line) and 90% super P +10% PVDF (blue solid line) electrodes in O_2-staurated atmosphere. CV of 80% ZZFC+10% super P+10% PVDF electrode in N_2-saturated atmosphere (red dash line). The scan rate was set at 0.1 V s^{-1}.

conductivities of the samples sintered at various temperatures are compared in Table 1. As expected, the conductivity increases with the sintering temperature.

The porous structure can be reflected by the N_2 adsorption−desorption isotherms, as presented in Figure 1. The original Fe(III)-MOF-5 sample contains both micropores of the framework and macropores between the crystalline particles. Accordingly, it shows a typical adsorption isotherm of

DOI: 10.1021/am509143t
ACS Appl. Mater. Interfaces 2015, 7, 4947−4954

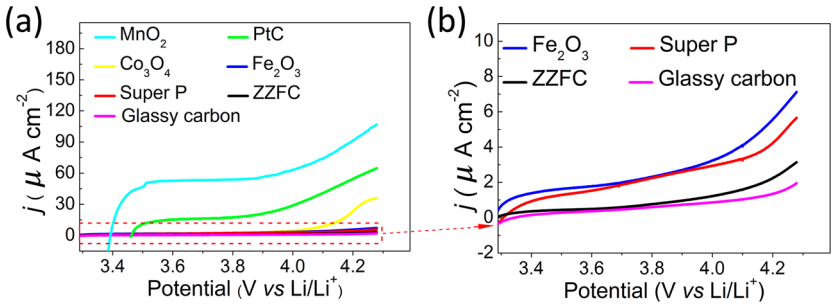

Figure 4. (a,b) LSV curves measured on rotating glassy carbon electrode coated with various air-electrode materials (the sweep rate was set at 0.01 V s^{-1} without rotation; panel b is the magnified image of panel a).

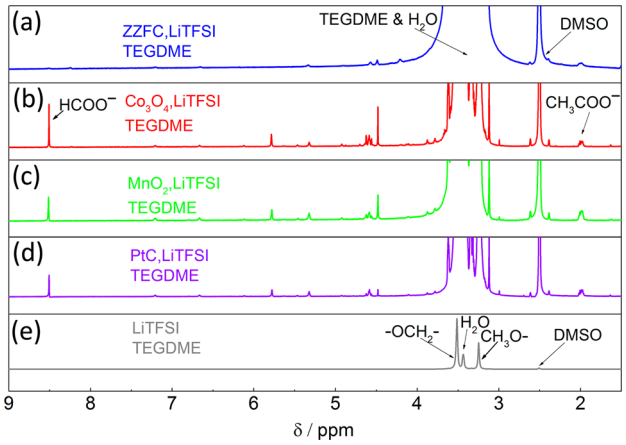

Figure 5. Magnified ^{1}H NMR spectra of the electrolytes in various cathodes after cycling (the cathode catalyst in each sample is (a) ZZFC, (b) Co_3O_4, (c) MnO_2, and (d) 5% PtC; all the aforementioned spectra are presented after magnified). (e) Nonmagnified ^{1}H NMR spectra of 1.0 mol l^{-1} LiTFSI in TEGDME solution.

microporous material (Figure 1a). After sintering, the organic compounds were carbonized and micropores of the MOF would collapse. Eventually, the material became mesoporous. The samples after sintering at 400, 450, and 500 °C show a similar type IV isotherm with H4 type hysteresis loop (IUPAC classification, Figure 1b,c,d), suggesting that the mesoporous structure of the samples was maintained up to 500 °C. Nevertheless, with further increasing sintering temperature, the hysteresis loop shrinks and the total quantity of adsorption significantly decreases (Figure 1e,f), demonstrating an evident destruction of the mesoporous structure. Therefore, in order to obtain a lithium−oxygen cathode with both good conductivity and proper porosity, the sintering temperature was chosen at 500 °C. The calculated BET surface area of the final ZnO/$ZnFe_2O_4$/C nanocages is 100.3 m^2 g^{-1}, and the average pore size is about 12.2 nm (Figures 1d and S1, Supporting Information).

The TG analysis carried out under N_2 atmosphere gives us an insight into thermal decomposition process of the Fe(III)-MOF-5. As shown in Figure S2a (Supporting Information), the mass plateau appears at 500 °C, confirming that the organic ligands in Fe (III)-MOF-5 are completely carbonized in N_2. The CV curves for the samples sintered at different temperatures are compared in Figure S3 (Supporting Information). We can see that the sample sintered at 500 °C has the highest peak current and lowest overpotential for both ORR and OER reactions. It confirms that 500 °C is an appropriate temperature for heat treatment.

The SEM images reveal that the Fe(III)-MOF-5 exhibits a well-defined uniform octahedral cage-like structure with average particle size around 200 nm (Figure 2a). The ZZFC obtained after sintering retains the same hollow cage structure (Figure 2b). From the TEM images (Figure 2c,d), we can obviously see the porous frameworks that construct the hollow octahedral cage. Figure 2e reveals that a very thin carbon layer is coated on the surface of the metal-oxide nanoparticles. The HR-TEM image (Figure 2f) clearly shows the lattice fringes; the distance between two adjacent plane (*d* value) are found to be 0.191 and 0.211 nm, which correspond to the (102) plane of ZnO and (400) plane of $ZnFe_2O_4$, respectively.

XPS measurement was applied to confirm the surface components and chemical element valence of the products. The survey scan spectrum (Figure 2g) suggests the presence of Zn, Fe, O, and C.[41] In the high-resolution XPS spectrum of Fe 2p (inset of Figure 2g), two obvious peaks appear at 711.3 eV for Fe $2p_{3/2}$ and 724.9 eV for Fe $2p_{1/2}$, together with an additional small satellite peak at 716.1 eV, which also corresponds to Fe^{3+}.[45,46] Figure 2h displays the XRD patterns of ZZFC. All diffraction peaks can be assigned to hexagonal ZnO (*P*63*mc*, $a = b = 0.3253$ nm, $c = 0.5213$ nm) and cubic $ZnFe_2O_4$ (*Fd*3*m*, $a = b = c = 0.84432$ nm), agreeing well with the XPS results. Thus, the ZZFC is confirmed to have many hollow cages that are composed of ZnO and $ZnFe_2O_4$ nanoparticles coated with thin carbon layers.

The presence of carbon derived from carbonization of organic ligands in Fe(III)-MOF-5 is evidenced by Raman spectroscopy (Figure S4, Supporting Information). Two typical Raman peaks located at 1363 and 1587 cm^{-1} are responsible for turbostratic and/or disordered carbonaceous features (D-band), and graphitic crystallites (G-band), respectively.[47] It is well-known that the *R* value (I_D/I_G) decreases with increasing amount of sp^2 (graphite) clusters in the sample.[48] The calculated *R*-value of ZZFC is 0.85, indicative of good conductivity. From the TG curve of ZZFC (Figure S2b, Supporting Information), the carbon content in the final sample is estimated to about 12 wt %.

The kinetics of the electrochemical process of ZZFC cathodes was investigated by CV (Figure 3). In the absence of oxygen, the CV curve shows no obvious redox peak. In the presence of oxygen, the ORR onset potential of the ZZFC electrode is approximately 2.8 V vs Li/Li^+, about 100 mV higher than that of the pure super P electrode. And a large increase in the peak current density obtained for both ORR and OER indicates the catalysis activity of ZZFC electrode.

To investigate the stability of the electrolyte, we designed a set of electrochemical LSV and NMR experiments. The LSV tests performed here were directly scanned from 3.38 to 4.28 V

DOI: 10.1021/am509143t
ACS Appl. Mater. Interfaces 2015, 7, 4947−4954

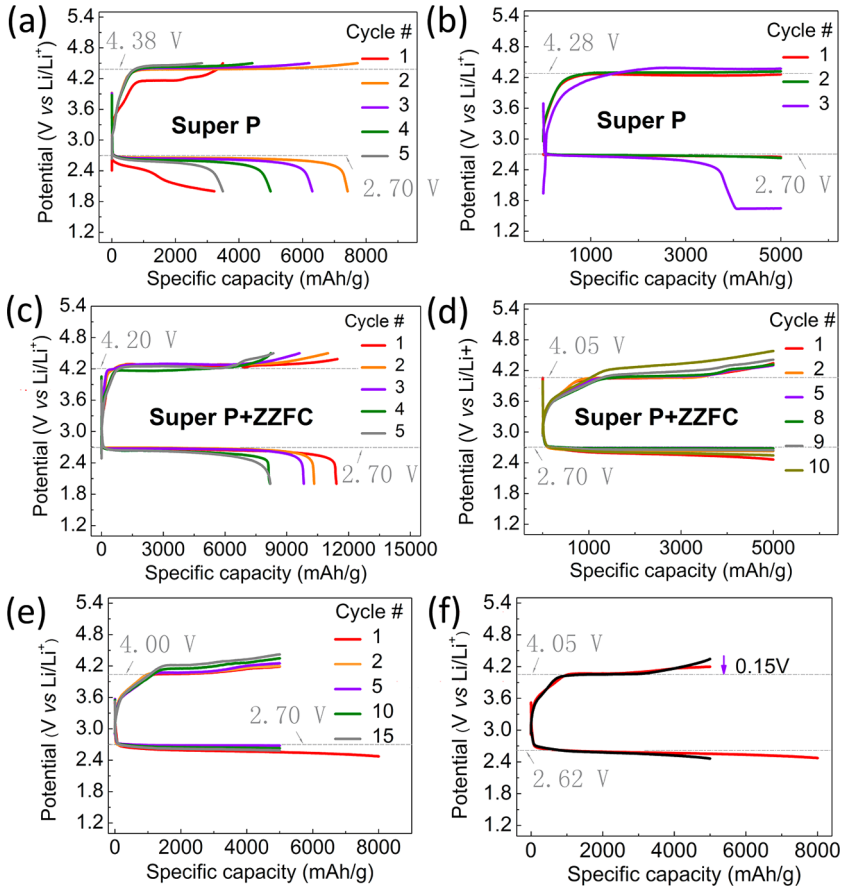

Figure 6. (a,b) Full voltage-range (a) and fixed capacity (b) galvanostatic discharge/charge curves of super P cathode (90% super P + 10% PVDF). (c,d) Full voltage-range (c) and fixed capacity (d) galvanostatic discharge/charge curves of ZZFC cathode (80% ZZFC + 10% PVDF + 10% super P). (e) Galvanostatic discharge/charge curves of ZZFC cathode in a "deep discharge + fixed capacity" mode. The cell was first discharged to 8000 mAh g^{-1}, and then cycled at fixed capacity of 5000 mAh g^{-1}. (f) Comparison of the discharge and charge curves of the first cycle using different cycling mode: red line: "deep discharge then fix capacity" mode as in panel e, black line: "fix capacity" mode as in panel d. The current density in all of these experiments was 300 mA g^{-1}.

(vs Li/Li^+) with different cathodic catalysts. In such a scan, since no Li_2O_2 is formed on the electrode before or during scanning, the current can only resulted from side reactions such as electrolyte oxidation or cathode decomposition. The current responses of Co_3O_4, MnO_2, and 5% PtC are much higher than those of Fe_2O_3, super P, ZZFC, and glassy carbon (Figure 4a), indicating that these traditional strong catalysts for fuel cells may catalyze the oxidation of electrolyte or cathode materials at high potential in oxygen atmosphere. It is worth noting that the current density of ZZFC is almost on a par with that of bare glassy carbon (Figure 4b), indicative of less side reaction occurred on the ZZFC electrode in TEGDME-based electrolyte.

^1H NMR spectra of the electrolytes after cycling with various cathodes ZZFC, MnO_2, Co_3O_4, and 5%Pt/C are compared in Figure 5. Before testing, all the cathodes were first discharged to 1.0 mAh, then recharged to 4.38 V. The decomposition products of TEGDME, such as Li formate and Li acetate,[33,49] can be clearly identified in the samples with MnO_2, Co_3O_4, and 5%Pt/C catalysts. While in the spectroscopy of the electrolyte of the ZZFC sample, at a same magnification ratio, the peaks from these byproducts are almost not observable. The water contamination (3.4 ppm) was brought in during the sample preparation process. The NMR results are consistent with the LSV results.

The galvanostatic discharge−charge performance of ZZFC cathodes was examined in coin-type lithium−oxygen batteries and compared with the pure super P in TEGDME-based electrolyte. Galvanostatic measurements were carried out in a voltage window between 2.0 and 4.5 V at a current density of 300 mA g^{-1}. The typical charge/discharge profiles are presented in Figure 6a,c. The ZZFC electrode delivers a discharge capacity of 11 410 mAh g^{-1} (calculated based on the total weight of the electrode, including super P and active material), which is much higher than the cell with pure super P electrode (7500 mAh g^{-1} at the second discharge cycle). In contrast, the charge plateaus of ZZFC electrode and the pure super P electrode are 4.26 and 4.41 V, respectively. We also explored the cycling performance of the as-prepared electrode by keeping the capacity at 5000 mAh g^{-1} (Figure 6b,d). For the pure super P electrode, the cell failed at the 3th cycle. For the ZZFC electrode, the discharge curve presented a plateau at 2.7 V but dropped to 2.6 V after 10 cycles; the charge end potential kept steadily over the initial 8 cycles but then increased soon in the 9th and 10th cycles.

Because high charging overpotential leads to fast electrolyte decomposition, lowering charge overpotential can help to improve the cyclability. To do so, we applied a "deep discharge + fixed capacity" mode in the galvanostatic test. The cell was first discharged to 8000 mAh g^{-1}, and then cycled at a fixed

DOI: 10.1021/am509143t
ACS Appl. Mater. Interfaces 2015, 7, 4947−4954

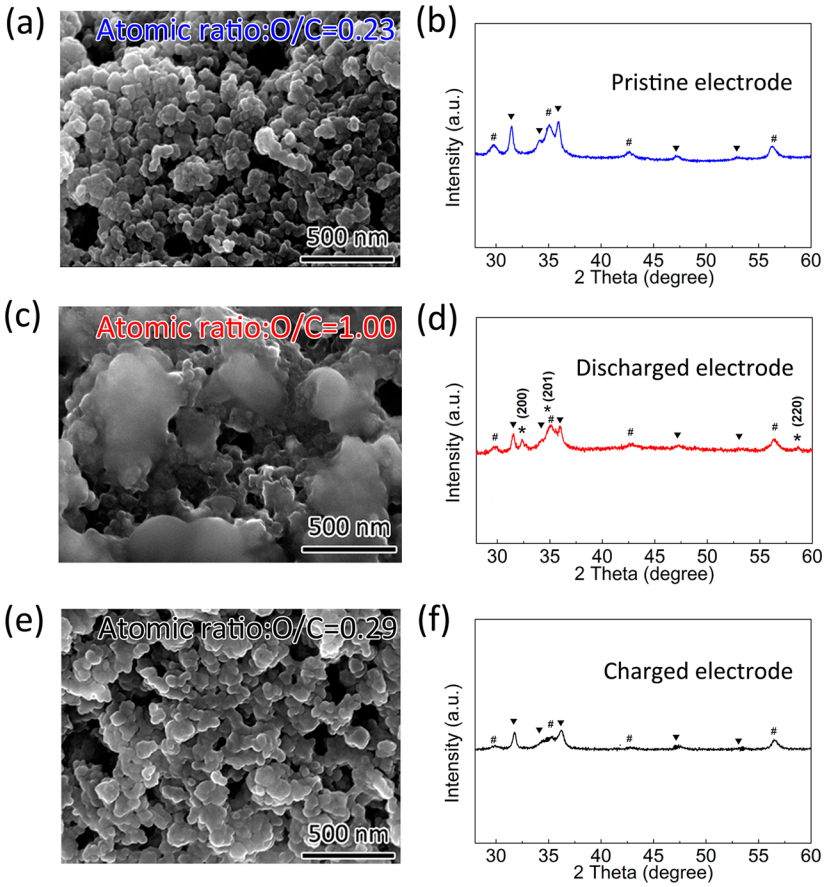

Figure 7. SEM images (a,c,e) and corresponding XRD patterns (b,d,f) for the ZZFC cathodes: (a,b) before discharge, (c,d) after discharged, and (e,f) after charge. Inset atomic ratios were obtained with EDX. Symbols in the XRD patterns indicate the ascription of the peaks: # ZnO,▼ $ZnFe_2O_4$, * Li_2O_2.

capacity of 5000 mAh g^{-1} (Figure 6e). This mode is designed based on the following considerations: the side reactions cannot be completely eliminated, and the discharge product is not pure lithium peroxide; moreover, the lithium peroxide cannot be fully oxidized in the charging process. Thereby, if the charging capacity was set equal to the discharge one, as what the conventional method does, the capacity produced by the lithium peroxide oxidation cannot fulfill the charging capacity. In the end part of the charging process, the charge capacity only comes from the side reactions. In other words, more side reactions are forced to happen at higher potential because there is not enough lithium peroxide left. However, in our "deep discharge + fixed capacity" mode, there are some "extra" lithium peroxide formed during the first discharge process. In the following cycles, the extra lithium peroxide can still be oxidized to avoid the high-potential side reactions at the end of charge process. Figure 6f shows that the charge end potential drops 0.15 V in the first cycle by using the"deep discharge + fixed capacity" mode. Accordingly, the cell can be operated at 5000 mAh g^{-1} for 15 cycles.

The composition change of the cathodes during cycling was tested with SEM, XRD, and EDX analysis (Figure 7). As presented in Figure 6d, three characteristic peaks corresponding to the Li_2O_2 phase were observed after fully discharged to 2 V. Because lithium and oxygen atoms are much lighter as compared with zinc and iron atoms, the Li_2O_2 diffraction peaks appeared not very strong. The EDX result suggests that atom percent of O/C element in the cathodes increased from 0.23 to 1.00 after discharge, which further proves that Li_2O_2 is the dominant discharge product. Observed from the SEM image (Figure 7c), we find that the Li_2O_2 product deposits on both the ZZFC electrode surface and the Li_2O_2 itself until the Li_2O_2 almost fills the space between the ZZFC electrode. This morphology demonstrates that the deposited Li_2O_2 does not block the catalytically active surface in the ZZFC electrode.[50] When the cell was recharged to 4.5 V, the characteristic peaks of Li_2O_2 disappeared (Figure 7f), suggesting that most of Li_2O_2 product can be oxidized on charging. Attributed to a small portion of undecomposed Li_2O_2, the atom percent of O/C in the charge electrode is slightly higher than that of the pristine electrode. Furthermore, we can see from the SEM image of the electrode sheet after running for 10 cycles (Figure S8d, Supporting Information) that the mesopores of the ZZFC are choked by the undecomposed Li_2O_2 and a small amount of side-reaction products. This should be the main reason for the performance decay.

Ideally, a lithium−oxygen battery cathode should contain a catalyst that can facilitate both ORR and OER but does not catalyze the oxidation of electrolyte or the decomposition of itself. However, there is a problem for this kind of ideal catalyst. In general, strong ORR/OER catalysts may chemically adsorb oxygen atoms and lower the energy barrier of the unstable intermediates. Such reactive sites may also adsorb electron donor groups on organic solvent molecules and weaken the chemical bonds near the adsorpted atoms. The intermediate species such as superoxide ions may easily oxidize the adsorbed

DOI: 10.1021/am509143t
ACS Appl. Mater. Interfaces 2015, 7, 4947−4954

molecules. Thus, it is very difficult to design such highly selective catalyst. But before that, we need to find some balance between the catalytic activity and the electrochemical stability. The overpotential of our cells indicates that the catalytic activity of ZZFC is not strong. However, owing to its excellent stability with the electrolyte and its rational porous architecture, it still delivers a relatively high reversible capacity.

4. CONCLUSIONS

Hierarchical mesoporous ZZFC nanocages were attained by pyrolyzing the Fe(III)-MOF-5 templates, and evaluated as cathode materials for lithium−oxygen batteries. By controlling the heat treatment condition, the porosity and conductivity of ZZFC were optimized to best fit the requirements of the air electrode. The ZZFC cathode exhibits large specific capacity and good cycling performance. We ascribe the outstanding performance of ZZFC to the following reasons: (1) ZZFC contains a rational architecture with combined characteristics of large surface area, hierarchical porosity and uniformly dispersed active sites, which benefits the mass/electron transportation in the multiphase discharge/charge reactions; (2) confirmed by LSV and NMR measurements, the TEGDME-based electrolyte is stable with the ZZFC during operation. Reduced parasitic reactions lead to reversible formation/decomposition of discharge product Li_2O_2. Our results demonstrate that balancing the conductivity and porosity, the catalytic activity and electrochemical stability is an efficient strategy to improve the cathodic performance for lithium−oxygen batteries.

■ ASSOCIATED CONTENT

Supporting Information

Preparation of α-MnO_2 nanowires/Co_3O_4 nanoflakes/Fe_2O_3 nanoflakes. (Figure S1) Pore-size distribution of the as prepared ZZFC obtained in the N_2 atmosphere at 500 °C. (Figure S2) Thermogravimetric (TG) analysis curve of (a) Fe(III)-modified MOF-5 obtained in the nitrogen flow; (b) ZZFC obtained in the air flow, with heating rate of 10 °C min^{-1}. (Figure S3) CVs of the samples after sintering Fe(III)-MOF-5 in N_2 at various temperatures: 400 °C (green line), 450 °C (red line), 500 °C (black line), 550 °C (blue line), and 600 °C (magenta line). (Figure S4) Raman spectrum of Fe(III)-MOF-5 and ZZFC. (Figure S5) XRD patterns of the Fe(III)-MOF-5. (Figure S6) SEM images of (a) α-MnO_2 nanowires (b) Co_3O_4 nanoflakes (c) Fe_2O_3 nanoflakes. (Figure S7) XRD patterns: (a) α-MnO_2 nanowires, (b) Co_3O_4 nanoflakes, and (c) Fe_2O_3 nanoflakes. (Figure S8) SEM images for the as-prepared ZZFC cathodes: (a) before cycling, (b) full discharge, (c) after charge, and (d) after 10 cycles. This material is available free of charge via the Internet at http://pubs.acs.org.

■ AUTHOR INFORMATION

Corresponding Authors

*Yunhui Huang. Tel./Fax: 027-87558241. E-mail: huangyh@hust.edu.cn.

*Yue Shen. E-mail: shenyue1213@hust.edu.cn.

Notes

The authors declare no competing financial interest.

■ ACKNOWLEDGMENTS

We acknowledge financial supports from the Natural Science Foundation of China (51202076). The authors thank the Analytical and Testing Center of HUST for TG, XRD, and FESEM measurements, and the State Key Laboratory of Materials Processing and Die & Mould Technology of HUST for BET, XRD, and TEM measurements.

■ REFERENCES

(1) Abraham, K. M.; Jiang, Z. A Polymer Electrolyte-based Rechargeable Lithium/Oxygen Battery. *J. Electrochem. Soc.* **1996**, *143*, 1−5.

(2) Bruce, P. G.; Freunberger, S. A.; Hardwick, L. J.; Tarascon, J. M. Li-O_2 and Li-S Batteries with High Energy Storage. *Nat. Mater.* **2012**, *11*, 19−29.

(3) McCloskey, B. D.; Scheffler, R.; Speidel, A.; Girishkumar, G.; Luntz, A. C. On the Mechanism of Nonaqueous Li−O_2 Electrochemistry on C and Its Kinetic Overpotentials: Some Implications for Li−Air Batteries. *J. Phys. Chem. C* **2012**, *116*, 23897−23905.

(4) Xu, J.-J.; Wang, Z.-L.; Xu, D.; Zhang, L.-L.; Zhang, X.-B. Tailoring Deposition and Morphology of Discharge Products Towards High-Rate and Long-Life Lithium-Oxygen Batteries. *Nat. Commun.* **2013**, *4*, 1−10.

(5) Peng, Z.; Freunberger, S. A.; Hardwick, L. J.; Chen, Y.; Giordani, V.; Barde, F.; Novak, P.; Graham, D.; Tarascon, J.-M.; Bruce, P. G. Oxygen Reactions in a Non-aqueous Li^+ Electrolyte. *Angew. Chem.* **2011**, *123*, 6475−6479.

(6) Laoire, C. O.; Mukerjee, S.; Abraham, K. M. Elucidating the Mechanism of Oxygen Reduction for Lithium-Air Battery Applications. *J. Phys. Chem. C* **2009**, *113*, 20127−20134.

(7) Yoo, E.; Zhou, H. Li-Air Rechargeable Battery Based on Metal-Free Graphene Nanosheet Catalysts. *ACS Nano* **2011**, *5*, 3020−3026.

(8) Xiao, J.; Mei, D.; Li, X.; Xu, W.; Wang, D.; Graff, G. L.; Bennett, W. D.; Nie, Z.; Saraf, L. V.; Aksay, I. A.; Liu, J.; Zhang, J. G. Hierarchically Porous Graphene as a Lithium-Air Battery Electrode. *Nano Lett.* **2011**, *11*, 5071−5078.

(9) Jian, Z.; Liu, P.; Li, F.; He, P.; Guo, X.; Chen, M.; Zhou, H. Core-Shell-Structured CNT@RuO_2 Composite as a High-Performance Cathode Catalyst for Rechargeable Li-O_2 Batteries. *Angew. Chem., Int. Ed.* **2014**, *53*, 442−446.

(10) Shen, Y.; Sun, D.; Yu, L.; Zhang, W.; Shang, Y.; Tang, H.; Wu, J.; Cao, A.; Huang, Y. A High-Capacity Lithium−Air Battery with Pd Modified Carbon Nanotube Sponge Cathode Working in Regular Air. *Carbon* **2013**, *62*, 288−295.

(11) Wang, Z.-L.; Xu, D.; Xu, J.-J.; Zhang, L.-L.; Zhang, X.-B. Graphene Oxide Gel-Derived, Free-Standing, Hierarchically Porous Carbon for High-Capacity and High-Rate Rechargeable Li-O_2 Batteries. *Adv. Funct. Mater.* **2012**, *22*, 3699−3705.

(12) Li, L.; Manthiram, A. O- and N-Doped Carbon Nanowebs as Metal-Free Catalysts for Hybrid Li-Air Batteries. *Adv. Energy Mater.* **2014**, *4*, 1301795.

(13) Cui, Y. M.; Wen, Z. Y.; Liang, X.; Lu, Y.; Jin, J.; Wu, M. F.; Wu, X. W. A Tubular Polypyrrole based Air Electrode with Improved O_2 Diffusivity for Li-O_2 Batteries. *Energy Environ. Sci.* **2012**, *5*, 7893−7897.

(14) Cui, Y.; Wen, Z.; Liu, Y. A Free-Standing-Type Design for Cathodes of Rechargeable Li−O_2 Batteries. *Energy Environ. Sci.* **2011**, *4*, 4727−4734.

(15) Xu, J.-J.; Wang, Z.-L.; Xu, D.; Meng, F.-Z.; Zhang, X.-B. 3D Ordered Macroporous $LaFeO_3$ as Efficient Electrocatalyst for Li−O_2 Batteries with Enhanced Rate Capability and Cyclic Performance. *Energy Environ. Sci.* **2014**, *7*, 2213−2219.

(16) Li, L.; Chai, S.-H.; Dai, S.; Manthiram, A. Advanced Hybrid Li−Air Batteries with High-Performance Mesoporous Nanocatalysts. *Energy Environ. Sci.* **2014**, *7*, 2630−2636.

(17) Li, L.; Manthiram, A. Decoupled Bifunctional Air Electrodes for High-Performance Hybrid Lithium-Air Batteries. *Nano Energy* **2014**, *9*, 94−100.

(18) Lu, Y.; Wen, Z.; Jin, J.; Cui, Y.; Wu, M.; Sun, S. Mesoporous Carbon Nitride Loaded with Pt Nanoparticles as a Bifunctional Air Electrode for Rechargeable Lithium-Air Battery. *J. Solid State Electrochem.* **2012**, *16*, 1863−1868.

DOI: 10.1021/am509143t
ACS Appl. Mater. Interfaces 2015, 7, 4947−4954

(19) Shao, Y.; Ding, F.; Xiao, J.; Zhang, J.; Xu, W.; Park, S.; Zhang, J.-G.; Wang, Y.; Liu, J. Making Li-Air Batteries Rechargeable: Material Challenges. *Adv. Funct. Mater.* **2013**, *23*, 987−1004.
(20) Li, F.; Zhang, T.; Zhou, H. Challenges of Non-aqueous Li−O_2 Batteries: Electrolytes, Catalysts, and Anodes. *Energy Environ. Sci.* **2013**, *6*, 1125−1141.
(21) Kwabi, D. G.; Ortiz-Vitoriano, N.; Freunberger, S. A.; Chen, Y.; Imanishi, N.; Bruce, P. G.; Shao-Horn, Y. Materials Challenges in Rechargeable Lithium-Air Batteries. *MRS Bull.* **2014**, *39*, 443−452.
(22) Xu, W.; Hu, J.; Engelhard, M. H.; Towne, S. A.; Hardy, J. S.; Xiao, J.; Feng, J.; Hu, M. Y.; Zhang, J.; Ding, F.; Gross, M. E.; Zhang, J.-G. The Stability of Organic Solvents and Carbon Electrode in Nonaqueous Li-O_2 Batteries. *J. Power Sources* **2012**, *215*, 240−247.
(23) Black, R.; Lee, J. H.; Adams, B.; Mims, C. A.; Nazar, L. F. The Role of Catalysts and Peroxide Oxidation in Lithium-Oxygen Batteries. *Angew. Chem.* **2013**, *125*, 410−414.
(24) Lu, Y.-C.; Shao-Horn, Y. Probing the Reaction Kinetics of the Charge Reactions of Nonaqueous Li−O_2 Batteries. *J. Phys. Chem. Lett.* **2013**, *4*, 93−99.
(25) Kwabi, D. G.; Batcho, T. P.; Amanchukwu, C. V.; Ortiz-Vitoriano, N.; Hammond, P.; Thompson, C. V.; Shao-Horn, Y. Chemical Instability of Dimethyl Sulfoxide in Lithium−Air Batteries. *J. Phys. Chem. Lett.* **2014**, *5*, 2850−2856.
(26) Itkis, D. M.; Semenenko, D. A.; Kataev, E. Y.; Belova, A. I.; Neudachina, V. S.; Sirotina, A. P.; Havecker, M.; Teschner, D.; Knop-Gericke, A.; Dudin, P.; Barinov, A.; Goodilin, E. A.; Shao-Horn, Y.; Yashina, L. V. Reactivity of Carbon in Lithium-Oxygen Battery Positive Electrodes. *Nano Lett.* **2013**, *13*, 4697−4701.
(27) McCloskey, B. D.; Scheffler, R.; Speidel, A.; Bethune, D. S.; Shelby, R. M.; Luntz, A. C. On the Efficacy of Electrocatalysis in Nonaqueous Li-O_2 Batteries. *J. Am. Chem. Soc.* **2011**, *133*, 18038−18041.
(28) Ottakam Thotiyl, M. M.; Freunberger, S. A.; Peng, Z.; Bruce, P. G. The Carbon Electrode in Nonaqueous Li-O_2 Cells. *J. Am. Chem. Soc.* **2013**, *135*, 494−500.
(29) McCloskey, B. D.; Speidel, A.; Scheffler, R.; Miller, D. C.; Viswanathan, V.; Hummelshøj, J. S.; Nørskov, J. K.; Luntz, A. C. Twin Problems of Interfacial Carbonate Formation in Nonaqueous Li−O_2 Batteries. *J. Phys. Chem. Lett.* **2012**, *3*, 997−1001.
(30) Xu, W.; Viswanathan, V. V.; Wang, D.; Towne, S. A.; Xiao, J.; Nie, Z.; Hu, D.; Zhang, J.-G. Investigation on the Charging Process of Li_2O_2-based Air Electrodes in Li−O_2 Batteries with Organic Carbonate Electrolytes. *J. Power Sources* **2011**, *196*, 3894−3899.
(31) Veith, G. M.; Dudney, N. J.; Howe, J.; Nanda, J. Spectroscopic Characterization of Solid Discharge Products in Li−Air Cells with Aprotic Carbonate Electrolytes. *J. Phys. Chem. C* **2011**, *115*, 14325−14333.
(32) McCloskey, B. D.; Bethune, D. S.; Shelby, R. M.; Girishkumar, G.; Luntz, A. C. Solvents' Critical Role in Nonaqueous Lithium−Oxygen Battery Electrochemistry. *J. Phys. Chem. Lett.* **2011**, *2*, 1161−1166.
(33) Freunberger, S. A.; Chen, Y.; Drewett, N. E.; Hardwick, L. J.; Barde, F.; Bruce, P. G. The Lithium-Oxygen Battery with Ether-based Electrolytes. *Angew. Chem., Int. Ed.* **2011**, *50*, 8609−8613.
(34) Peng, Z.; Freunberger, S. A.; Chen, Y.; Bruce, P. G. A Reversible and Higher-Rate Li-O_2 Battery. *Science* **2012**, *337*, 563−566.
(35) M, M.; Thotiyl, O.; Freunberger, S. A.; Peng, Z.; Chen, Y.; Liu, Z.; Bruce, P. G. A Stable Cathode for the Aprotic Li−O_2 Battery. *Nat. Mater.* **2013**, *12*, 1050−1056.
(36) Nørskov, J. K.; Rossmeisl, J.; Logadottir, A.; Lindqvist, L. Origin of the Overpotential for Oxygen Reduction at a Fuel-Cell Cathode. *J. Phys. Chem. B* **2004**, *108*, 17886−17892.
(37) Stamenkovic, V.; Mun, B. S.; Mayrhofer, K. J. J.; Ross, P. N.; Markovic, N. M.; Rossmeisl, J.; Greeley, J.; Nørskov, J. K. Changing the Activity of Electrocatalysts for Oxygen Reduction by Tuning the Surface Electronic Structure. *Angew. Chem.* **2006**, *118*, 2963−2967.
(38) Greeley, J.; Rossmeis, J.; Stephens, I. E. L.; Chorkendorff, I.; Bondarenko, A. S.; Nørskov, J. K.; Johansson, T. P.; Hansen, H. A. Alloys of Platinum and Early Transition Metals as Oxygen Reduction Electrocatalysts. *Nat. Chem.* **2009**, *1*, 552−556.
(39) Olivares-Marín, M.; Palomino, P.; Enciso, E.; Tonti, D. Simple Method to Relate Experimental Pore Size Distribution and Discharge Capacity in Cathodes for Li/O_2 Batteries. *J. Phys. Chem. C* **2014**, *118*, 20772−20783.
(40) Williford, R. E.; Zhang, J.-G. Air Electrode Design for Sustained High Power Operation of Li/Air Batteries. *J. Power Sources* **2009**, *194*, 1164−1170.
(41) Zhang, Z.; Chen, Y.; Xu, X.; Zhang, J.; Xiang, G.; He, W.; Wang, X. Well-Defined Metal−Organic Framework Hollow Nanocages. *Angew. Chem., Int. Ed.* **2013**, *126*, 439−443.
(42) Zou, F.; Hu, X.; Li, Z.; Qie, L.; Hu, C.; Zeng, R.; Jiang, Y.; Huang, Y. MOF-Derived Porous ZnO/$ZnFe_2O_4$/C Octahedra with Hollow Interiors for High-Rate Lithium-Ion Batteries. *Adv. Mater.* **2014**, *26*, 6622−6628.
(43) Wu, D.; Guo, Z.; Yin, X.; Pang, Q.; Tu, B.; Zhang, L.; Wang, Y.-G.; Li, Q. Metal−Organic Frameworks as Cathode Materials for Li−O_2 Batteries. *Adv. Mater.* **2014**, *26*, 3258−3262.
(44) Chen, W.; Zhang, Z.; Bao, W.; Lai, Y.; Li, J.; Gan, Y.; Wang, J. Hierarchical Mesoporous γ-Fe_2O_3/Carbon Nanocomposites Derived From Metal Organic Frameworks as a Cathode Electrocatalyst for Rechargeable Li-O_2 Batteries. *Electrochim. Acta* **2014**, *134*, 293−301.
(45) Yamashita, T.; Hayes, P. Analysis of XPS Spectra of Fe^{2+} and Fe^{3+} Ions in Oxide Materials. *Appl. Surf. Sci.* **2008**, *254*, 2441−2449.
(46) Cao, Z.; Wei, B. High Rate Capability of Hydrogen Annealed Iron Oxide-Single Walled Carbon Nanotube Hybrid Films for Lithium-Ion Batteries. *ACS Appl. Mater. Interfaces* **2013**, *5*, 10246−10252.
(47) Bordjiba, T.; Mohamedi, M.; Dao, L. H. New Class of Carbon-Nanotube Aerogel Electrodes for Electrochemical Power Sources. *Adv. Mater.* **2008**, *20*, 815−819.
(48) Hou, L.; Lian, L.; Li, D.; Pang, G.; Li, J.; Zhang, X.; Xiong, S.; Yuan, C. Mesoporous N-Containing Carbon Nanosheets towards High-Performance Electrochemical Capacitors. *Carbon* **2013**, *64*, 141−149.
(49) Black, R.; Oh, S. H.; Lee, J.-H.; Yim, T.; Adams, B.; Nazar, L. F. Screening for Superoxide Reactivity in Li-O_2 Batteries: Effect on Li_2O_2/LiOH Crystallization. *J. Am. Chem. Soc.* **2012**, *134*, 2902−2905.
(50) Sun, D.; Shen, Y.; Zhang, W.; Yu, L.; Yi, Z.; Yin, W.; Wang, D.; Huang, Y.; Wang, J.; Wang, D.; Goodenough, J. B. A Solution-Phase Bifunctional Catalyst for Lithium-Oxygen Batteries. *J. Am. Chem. Soc.* **2014**, *136*, 8941−8946.

DOI: 10.1021/am509143t
ACS Appl. Mater. Interfaces 2015, 7, 4947−4954